Optimization of n-PERT Solar Cell under Atacama Desert Solar Spectrum

Pablo Ferrada Martínez

Centro de Desarrollo Energético Antofagasta (CDEA), Universidad of Antofagasta, Av. Angamos 601, Antofagasta, Chile

Benjamín Ivorra

Interdisciplinary Mathematics Institute (IMI) and Department of Applied Mathematics and Mathematical Analysis, Complutense University of Madrid, Plaza de las Ciencias, 3, 28040 Madrid, Spain

Miriam Ruiz Ferrández

MOMAT Research Group, Complutense University of Madrid, Supercomputing-Algorithms Research Group, University of Almería, Spain

Emilio Ruiz Reina

Escuela de Ingenierías Industriales, Dep. Applied Physics II, University of Málaga, Spain

Abstract. Solar spectra in the Atacama Desert differs from the global standard, exhibiting very high irradiance values. In addition, the atmospheric composition leads also to high ultraviolet levels. These facts are mainly attributed to the latitude and low content of local atmospheric aerosols and ozone. Further, the response of photovoltaic (PV) solar cells to solar radiation is spectrally dependent. Consequently, it may be necessary to consider local conditions and type of technology to optimize PV devices, since solar cells are mostly designed for highest performance at standard testing conditions (STC). This work aims to optimize the output power of an n-type passivated emitter and rear totally diffused solar cell (n-PERT), when operating under a representative Atacama Desert solar spectrum, the AM 1.08 (AM stands for air mass). The solar cell model is based on the drift-diffusion and continuity equations implemented in the Semiconductor Module of COMSOL Multiphysics v6. The needed inputs were obtained by means of measurements and calculations. The calculated performance of the modeled solar cell was compared to the measured response for validation. Six optimization parameters were considered: emitter, base, and back surface field (BSF) thickness as well as emitter, base and BSF doping concentration. The selected parameters were optimized to STC and the AM1.08 spectrum by means of a genetic algorithm (GA) implemented in MATLAB. In the validation step, the short circuit current density, open circuit voltage and fill factor showed relative differences between calculated and measured values below 1% for front side illumination at STC. In the case of the output power the relative difference was up to 8%. After implementing the GA, the optimized thickness was 0.2 µm for the emitter, 150 µm for the cell and 0.25 µm for the BSF. The optimized doping concentration for each layer was 9.36×10^{19} cm^{-3}, 9.84×10^{14} cm^{-3} and 4.12×10^{20} cm^{-3}. The values found for the emitter and BSF are different to those at STC, highlighting the need of considering a local spectrum for the optimal design of solar cells.

I. INTRODUCTION

According to Solar GIS (see FIG. 1) [1], there are regions in the world such as North America, South America, southern Europe, Africa, and Oceania where the Global Horizontal Irradiation (GHI) exceeds 2000 kWh/m^2 per year. Particularly, the Atacama Desert accounts for the highest solar energy resource in the world [2–4].

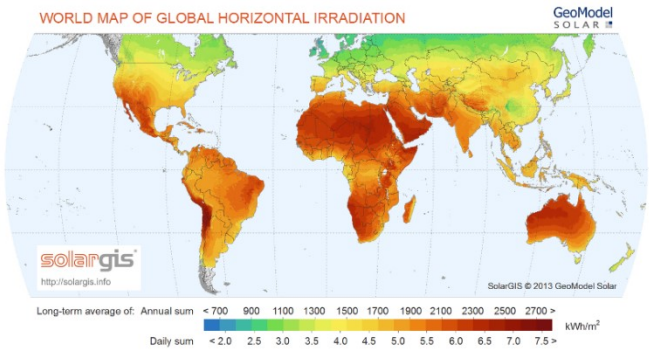

FIG. 1. Global Horizontal Irradiation map from Solar GIS [1].

To provide a deeper insight into the solar resource, the solar spectrum must be considered. Knowledge of the spectrum can be linked to several areas of research: the study of the atmospheric composition, ultraviolet (UV) content, and especially, for photovoltaic (PV) technology. The main reason for the latter is that solar cells response is dependent on the photon energy, and so the PV module, which is made of a collection of interconnected solar cells sandwiched between polymer based encapsulants and glass.

Photovoltaic cells and modules are usually measured under standard testing conditions (STC), which means that they are illuminated under a standard reference solar spectrum with 1000 W/m^2 and 25 °C. The American Society for Testing and Materials and research centers of the United States (U.S.) [5] supported the definition of the reference spectrum norm G173-03. The two main spectra defined under this scheme are the standards for direct normal and global tilted (at 37°) spectral irradiances [6] with an Air Mass of 1.5 (AM1.5). The corresponding atmospheric conditions are an average for the United States (U.S.) over one year. Considering the atmospheric composition, the standard spectral irradiances were calculated using the Simple Model of the Atmospheric Radiative Transfer of Sunshine (SMARTS) [7,8].

Following a similar approach, that is, based on atmospheric conditions and SMARTS, spectra associated to different locations can be computed. The abundant solar resource in northern Chile (FIG. 1) and the noticeable implementation of PV plants in this region have given an impulse to researchers to investigate the impact of the solar spectrum and environmental conditions to PV technologies. Based on these requirements, a mean spectrum for the Atacama Desert region

from the available long-term databases was calculated [9]. Thus, the mean direct and global spectral irradiances for the zone under study were estimated. Considering the standard AM1.5G (global) and the AM1.08 for the mean global tilted irradiance in the Atacama Desert, 5.6% of Reference Spectrum (AM1.5G) is UVA + UVB for the Tilted Global Irradiance (GTI); whereas the Atacama Desert receives the highest irradiation in the world, with 7.7% of its energy in the UV range. Alone this result can have implications in the operation of PV devices under real conditions of high irradiance and UV content. Additionally, degradation effects may be enhanced.

Considering the description regarding solar spectrum there are differences with respect to reference AM1.5. These differences refer mainly to intensity and UV content. Researchers found arguments to define a Desert Label for Atacama Desert [10]. These results highlight the need of knowing solar spectrum for specific locations, which may have implications in the definition of measurement standards and procedures for PV module durability tests.

Solar cell is designed for highest efficiency under standard testing conditions (STC): AM1.5G spectrum, 1000 W/m^2 and 25 °C. Since the solar spectrum varies during the day, solar cells in a PV module rarely operate at the optimum. In fact, the PV device exhibits losses when operating at non-standard conditions. Fundamental losses have been investigated in [11]. Authors highlight that the mismatch between solar spectrum and the mono-energetic absorption of a single bandgap leads to non-absorption of photons with energy below the bandgap. In addition, the mismatch between excited carriers and lattice phonons causes thermalization. Given that the mean GTI of Atacama Desert (AM1.08) exhibits higher intensity and UV content, it is possible to assert that thermalization losses can be even larger compared to the case at STC. As stated, thermal issues are crucial in the operation of solar cell devices, since it is associated to recombination phenomena, being temperature dependent [12].

The trend for industrial crystalline silicon (c-Si) solar cells is the bifacial concept, bringing the advantage of photon absorption from front and rear sides. The ITRPV [13] reports on state-of-the-art technologies such as the back surface field (BSF), passivated emitter and rear cell (PERC), passivated emitter and rear locally diffused solar cell (PERL), passivated emitter and rear totally diffused solar cell (PERT) and Si heterojunction (SHJ). The PERC/PERL/PERT group massified worldwide. Particularly, n-PERT bifacial solar cell achieved efficiencies of 22% with a bifaciality of 95% [14].

The aim of this work is to determine optimal parameters of a n-PERT solar cell (see cell structure in the inset of FIG. 1), when operating under Atacama spectral conditions. The next question to answer is how this theoretical and optimized solar cell performs during a whole day in the Atacama Desert. For this purpose, the power output obtained from the current-voltage (JV) characteristics is used in the optimization step.

II. MATERIALS AND METHODS

The approach to accomplish the goals of this work are summarized in 3 steps: 1) Validation, 2) optimization, 3) prediction. The validation consists of collecting empirical data, developing the model and compare experimental with numerical results, when illuminated with the standard spectrum. The optimization consists of finding optimum values of selected parameters for maximum power when illuminated with the mean Atacama Spectrum (AM1.08). See spectra in FIG. 2. The prediction refers to calculating the performance of the optimized cell for different spectra.

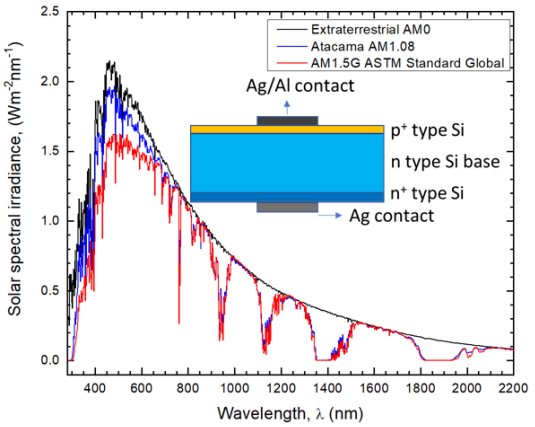

FIG. 2. Extraterrestrial AM0, Atacama Desert AM1.08 and reference AM1.5G solar spectrum. A sketch of the cell is in the inset.

A. Model validation

It consists of the fabrication of n-PERT solar cells, characterization, and results analysis. This part of the work has been done and the experimental details have been published by Ferrada et al in [15]. In that reference, details regarding geometry, doping level and output current-voltage characteristics are known. The doping profile of the emitter and BSF was simulated as gaussian, according to $N = N_0 \exp((-d/l)^2)$, where N_0 is the surface concentration, d is distance and $l = d_j/\sqrt{ln(\lceil N_0/N_b \rceil)}$ is the decay length. For the front and rear side of the cell, the metal fractions were $f_{met,f} = 0.052$ and $f_{met,r} = 0.099$. The metal fraction is defined as the ratio of the covered area by the metallization to the cell area. Values for the SRH carrier lifetimes were obtained from [16,17]. See details in Table 1.

Table 1: Input parameters obtained through measurements.

Name	Value	Description
d_{cell}	180 µm	Solar cell thickness
d_E	0.65 µm	Emitter depth
d_{BSF}	0.45 µm	Thickness of BSF
N_E	2.44×10^{19} cm^{-3}	Emitter surface conc.
N_B	8.436×10^{14} cm^{-3}	Base doping
N_{BSF}	6.17×10^{19} cm^{-3}	BSF surface conc.
τ_n	1.5 ms	SRH Carrier lifetime
τ_p	1.5 ms	SRH Carrier lifetime

In addition, the spectral reflectance (R_λ) of the metallized solar cell was carried out using a Perkin Elmer 950 Spectrophotometer (FIG. 3). More details are found in [18].

A 1D model was developed in the Semiconductor Module of COMSOL Multiphysics v6 and tested using the AM1.5g though a stationary study. Once the current-voltage characteristics (JV) are calculated, electrical outputs, i.e., the short circuit current density (J_{sc}), open circuit voltage (V_{oc}), fill factor (FF), power (P_{mpp}, where *mpp* stands for maximum power point) and efficiency (η) can be compared to the measured JV values. The measured and calculated JV curves at STC is shown in the Results and discussion section.

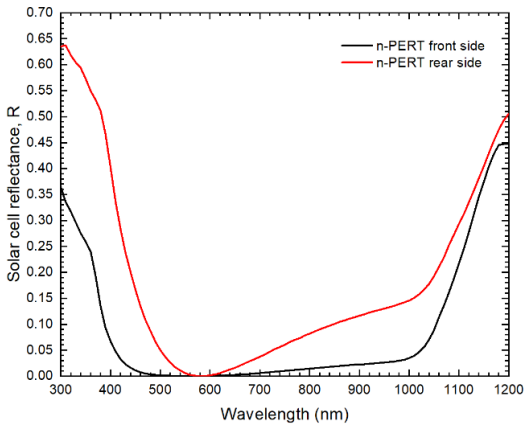

FIG. 3. Spectral reflectance of the n-PERT solar cell.

A mesh independence study was conducted to identify the minimum N° of elements, leading to satisfactory results. It means that an electrical output obtained with a certain N° of mesh elements does not vary significantly for more elements. The analysis was applied to J_{sc}, V_{oc}, P_{mpp} and η (see FIG. 4, where electrical outputs were normalized to those using the largest number of mesh elements). Above 600 mesh elements, the electrical outputs nearly match the ones computed with the extremely fine mesh. A fine mesh can be used as well since there is a variation only at the third significant figure.

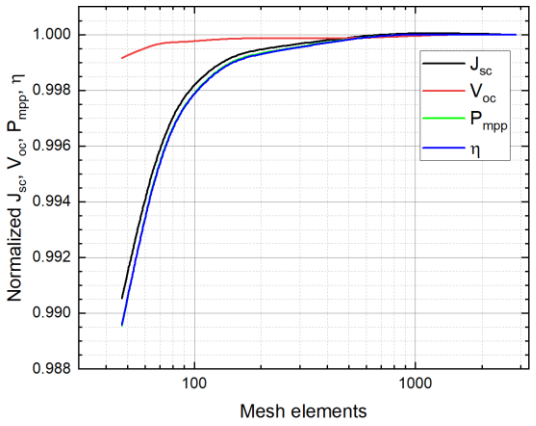

FIG. 4. Mesh independence study of the main output JV parameters as function of the mesh elements for a 1D model.

After completing the mesh study, any possible differences between the experimental results and the simulations are discussed and explained. There are mainly two sources of discrepancies between experiment and model:

(1) Since the model assumes flat surfaces, a correction factor was introduced to match J_{sc}. Nevertheless, the increase of surface area is accompanied by a larger saturation current density J_0 due to recombination. Authors [17] considered these issues and defined correction factors (f_{corr}) for different solar cells. To simulate J_{sc} at STC conditions, a factor $f = 1.17$ for the front side of the n-PERT was used, where $f_{corr} = J_{sc,meas}/J_{sc,cal}$. That is the ratio of the measured short circuit current density ($J_{sc,meas}$) to the calculated value ($J_{sc,cal}$).

(2) The model does not consider metal induced recombination. Therefore, V_{oc} may be higher than the experimental result. However, this differences were quantified and were fully described in [19]. Authors determined the reduction in the open circuit voltage ΔV_{oc} of n-PERT cells by varying the metal fraction f_{met} and quantifying the dark saturation current density at metal/semiconductor interfaces. For the metal fraction of n-PERT cells in this work, the V_{oc} decreases 45 mV due to the front side metallization and 35 mV due to the rear side metallization. In addition, the effect of series and shunt resistance (R_{ser} and R_{shunt}) is observable in the shape of the JV curve, and thus, on the FF and P_{mpp} [20]. Based on the referenced work, metal induced recombination can be applied after the model is solved, by subtracting ΔV_{oc} for the corresponding metal fraction. In addition, ohmic losses will affect P_{mpp} and FF. For power, $P_{mpp} = P_{mpp,0} - R_{ser} {I_{mpp}}^2$, where $P_{mpp,0}$ is the power without resistance effects. For the fill factor, $FF = FF_0(1 - r_{ser})$, where FF_0 is the fill factor without resistive effects, r_{ser} is the normalized series resistance to the characteristic resistance ($r_{ser} = R_{ser}/R_{CH}$ and $R_{CH} = V_{oc}/I_{sc}$) [21].

C. Optimization

It consists of the definition of the objective function, control parameters, constraints, and output variable. The mph COMSOL file was saved as *.m, only returning the output power as function of the control parameters. Six optimization parameters were defined to maximize the output power of the solar cell. These parameters were the emitter (d_E), cell (d_{cell}), and back surface field (d_{BSF}) thickness as well as emitter (N_E), base (N_B) and BSF (N_{BSF}) doping concentration. To find the optimum parameters, a genetic algorithm (GA) was used. The main stages of the GA are described [22].

i. Randomly to produce a first generation of individuals in the search space Ω. It means, given a fixed population size $N_p \in \mathbb{N}$, there are N_p points randomly generated, where the set is written as: $X^0 = \left\{x_1^0, \dots, x_{N_p}^0, \text{such that } x_1^0 \in \Omega,\ i = 1 \dots N_p\right\}$. X^0 is called the initial generation (generation 0).

ii. During a fixed number of iterations $N_g \in \mathbb{N}$, called generations, several sub processes occur. For each generation $n = 0 \dots N_g$, considering X^n, following processes take place:

a. Selection: the value of the cost function g of all x_i^n points are calculated, and it is denoted as $g_i^n = g(x_i^n)$, with $i = 1, \dots N_p$. To each x_i^n, a probability p_i^n to be selected, is assigned. The probability can be written in terms of the cost function, $p_i^n = p(g_k^n)$. Once the probability is computed, $2N_p$ elements called parents are chosen and they are denoted as y_i^n, with $i = 1, \dots 2N_p$. This procedure assumes that the region of the points with the lowest value of g is explored with a larger frequency.

b. Crossover: N_p elements called children are created. They are denoted as e_i^n, with $i = 1, \dots N_p$, from the values of the parents y_i^n. This step is intended to explore a zone included between two parents' points and determine if there is a better element.

c. Mutation: Some components of the e_i^n elements are randomly modified. The goal is to explore some zones of the search space randomly. In addition, this step allows to escape from possible local minima, which may bring too many elements of the population.

d. Elitism: To ensure that the convergence of the GA is always decreasing, that is, the value of g of the best element from each generation is decreasing from one generation to another. Thus, the best element of the previous generation X^n is directly copied and it is denoted as $\bar{x}^n$.

After implementing these steps, the next generation $X^{n+1} = \{e_1^n, \dots, e_{N_p}^n\}$ is obtained. Once the GA is finished, it leads to the point $\bar{x}^n$, where n is the last calculated generation. This solution is an approximation for the optimization problem. In general, this algorithm can rapidly find a zone near the global optimum. However, it can lack of precision [23]. To improve the precision, a hybridization with another algorithm can lead to a more accurate solution. For instance, the gradient descent method (or steepest descent method). See an example in [24].

Once defined the algorithm, one needs to choose the parameters: N_p, N_g, p_m, and if it applies, the parameters of the algorithm for hybridization. Additionally, the stop tests are defined. If during N_s iterations, the value of $\bar{x}^n$ remain unchanged, the GA is stopped. Once the solution is obtained, a convergence curve is constructed.

D. Prediction

It consists of using the optimized solar cell parameters to execute the model for different solar spectra received in Atacama with the associated cell temperature. The COMSOL file was modified to include a Java code. A description of (i) spectra, (ii) temperature and (iii) Java is provided:

(i) The solar spectra were determined using SMARTS (Simple Model of the Atmospheric Radiative Transfer of Sunshine) [25]. The SMARTS needs local atmospheric parameters to calculate the atmospheric spectral transmittance at a given place and time. The spectra were obtained for a representative location, the Atacama Desert Solar Platform (PSDA) with coordinates 24.090S, 69.929W, for the summer solstice of December 21st, 2018. The PSDA is a facility to test solar technologies, hosting a meteorological station to measure inputs for SMARTS. See [26] for details. The spectra of the solstice day for calculations are presented in FIG. 5.

These spectra refer to the spectral global tilted irradiance (GTI_λ) and denoted as F for COMSOL calculations. It was obtained for the front and rear side of PV modules installed with north orientation at 20° tilt (FIG 5a and 5b), and with east orientation at 90° tilt (FIG. 5c and 5d). The GTI_λ spectra were determined at each hour between 7:00 h and 18:00 h in True Solar Time (TST).

(ii) Solar spectrum but also the solar cell temperature varies during the day. As described in the introduction, excess photon energy can lead to thermalization losses. In practical terms, the solar cell temperature varies depending on the solar irradiance and other factors such as ambient temperature and wind speed, among others. A method was proposed to obtain the solar cell temperature, ${T_c}^{LS}$, (where LS refers to least square), as a linear combination of the temperatures ${T_c}^t$, ${T_c}^S$, ${T_c}^C$, ${T_c}^L$ y ${T_c}^K$, according to Eq. 1 [27]. Each term in that equation was calculated using the climatological data from the PSDA for each hour of the day through a thermal balance [27]. The calculated cell temperature for the bifacial n-PERT cell at 20° and 90° tilt is shown in FIG. 6.

$$ {T_c}^{LS} = w_t {T_c}^t + w_S {T_c}^S + w_C {T_c}^C + w_L {T_c}^L + w_K {T_c}^K \quad (1) $$

The vertical orientation leads to a more uniform tendency during the day compared to the 20º tilted case. In both cases, maximum temperature is reached at 13:00 with 67.5°C and 44.4°C for 20° and 90° tilt respectively. The temperature provided below was used in the Arora model for mobility (see Theory section, where the general form of the equation is shown).

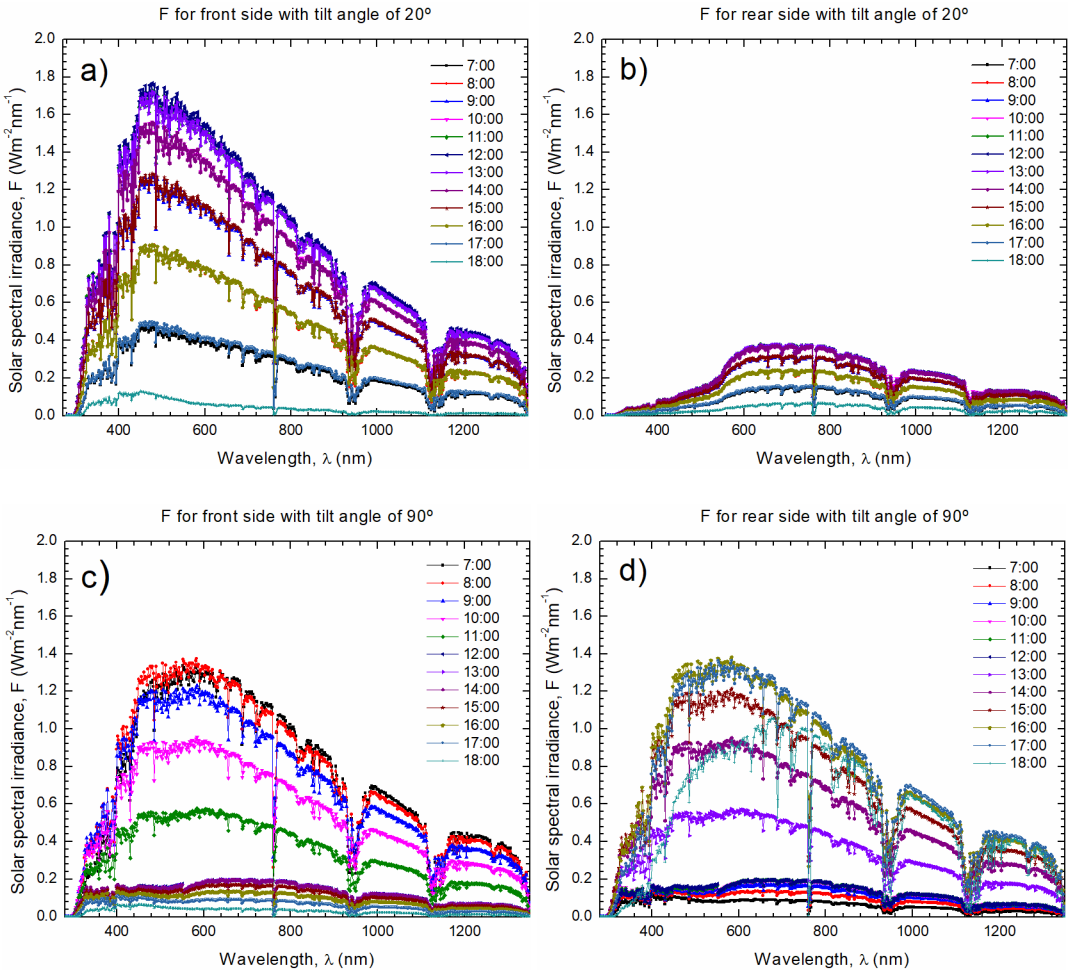

FIG. 5. (a) Solar spectral irradiance (GTI_λ) for the 20° tilted case, north-south oriented: (a) Front side and (b) Rear side. Solar spectral irradiance GTI_λ for the front side (c) and rear side (d) for the 90° tilted case. Calculations are in Local True Solar Time (LTST).

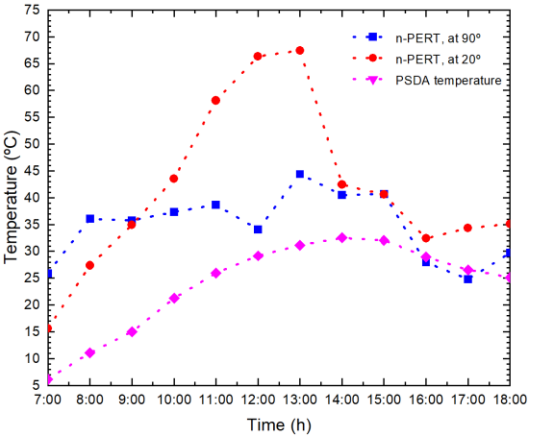

FIG. 6. Solar cell temperature for the 90° and 20° tilt angles as well as ambient temperature at the PSDA location for comparison.

(iii) The Java method was included in the Application Builder and reads the solar spectra of FIG. 5 and solar cell temperature of FIG. 6. The method acts on a matrix, where the information is organized according to Table 2. Let a_{ij} be an element of the matrix. The first row (a_{0j} elements), with $j = 1, \dots, 12$, contain the temperatures associated to each solar spectrum for each hour during the day. The a_{ij} elements with $i > 0$ and $j = 1, \dots, 12$ comprise solar spectra, where the wavelength values are in the first row (a_{0j} elements).

Table 2: Structure of the table to import in COMSOL, containing solar cell temperature and solar spectra.

Temperature	T_c1	…	T_c12
300	Spectrum 1	…	Spectrum 12
.			
.			
.			
1200			

The Java method allows for replacing a specific solar spectrum in the Generation Rate of electron-holes pairs, for a switch (sw) function. The sw function varies the index which is associated to a specific spectrum. In the following code, the index i runs up to 13 since there are 12 spectra for each side of the solar cell. Thus, sw1 is used for the front side, whereas sw2 is used for the rear side of the device. Cell temperature (T_c) is called writing sw(0) when temperature is required in the semiconductor interface, as T_c values are stored in the first row of the table in Table 2. The part of the method for the front illumination is shown in the following lines.

```
for (int i = 1; i < 13; ++i) {

  model.func("sw1").feature().create("int"+toString(i),
"Interpolation");
  with(model.func("sw1").feature("int"+toString(i)));
    set("source", "file");
    set("filename", "…\\spectrum.txt");
    set("nargs", 1);
    setIndex("funcs", "GTIf"+toString(i), 0, 0);
    setIndex("funcs", i, 0, 1);
  endwith();

  with(model.func("sw1").feature("int"+toString(i)));
    set("argunit", "nm");
  endwith();
  }
```

III. THEORY

The JV curve of the c-Si cells can be calculated through the net charge relation (i), the holes and electrons transport (ii) and continuity (iii) equations.

(i) Net charge density relation

The net charge density relation is $\nabla \cdot (-\varepsilon_r \nabla V) = \rho$, where ε_r is the relative permittivity of the semiconductor, V is the electric potential and ρ is the charge density given by $\rho = q(p - n + N_d^+ - N_a^-)$. In which q is the elementary charge carrier, n and p are the electron and hole concentration, and N_d^+ and N_a^- the ionized impurity concentration. See Eq. 2.

$$\nabla \cdot (-\varepsilon_r \nabla V) = \rho = q(p - n + N_d^+ - N_a^-) \tag{2}$$

(ii) Transport equations

The transport of electrons and holes in terms of the current densities J_n and J_p, are shown in Eq. 3 and Eq. 4, respectively. The quantities μ_n and μ_p are the electron and hole mobilities and E_C and E_V are the conduction and valence band edges. In addition, k_B is the Boltzmann's constant, T is the temperature, $\mathcal{G}$ is the ratio of the Fermi integrals, $\mathcal{G}(n/N_C) = \mathcal{F}_{1/2}(\zeta)/\mathcal{F}_{-1/2}(\zeta)$ with $\zeta = \mathcal{F}^{-1}{}_{1/2}(n/N_C)$, while N_C and N_V are the effective density of states in the conduction and valence bands, $D_{n,th}$ and $D_{p,th}$ are thermal diffusivities.

$$\boldsymbol{J_n} = qn\mu_n \nabla E_C + \mu_n k_B T \mathcal{G}\left(\frac{n}{N_C}\right)\nabla n + qnD_{n,th}\nabla \ln(T) \tag{3}$$

$$\boldsymbol{J_p} = qp\mu_p \nabla E_V - \mu_p k_B T \mathcal{G}\left(\frac{p}{N_V}\right)\nabla p - qpD_{p,th}\nabla \ln(T) \tag{4}$$

The first and second terms in Eq. 3 and Eq. 4 stand for the drift and diffusion model for electrons and holes; whereas the third term corresponds to corrections related to the Fermi-Dirac statistics [28]. The scattering of charge carriers due to impurities and phonons, is included through the Arora mobility model [29] (Eq. 5). This model includes the dependency on the impurities but also on cell temperature, as μ_{min}, μ_0 and m are T-dependent (see details in [30]).

$$\mu = \mu_{min} + \frac{\mu_0}{1 + \left(N/N_{ref}\right)^m} \tag{5}$$

(iii) Continuity equations

The continuity equations for electron and holes are Eq. 6 and 7, where U_n and U_p are the net electron and hole recombination rate, with $U_n = \sum R_{n,i} - \sum G_{n,i}$ and $U_p = \sum R_{p,i} - \sum G_{p,i}$, respectively.

$$\frac{\partial n}{\partial t} = \frac{1}{q}(\nabla \cdot \boldsymbol{J_n}) - U_n \tag{6}$$

$$\frac{\partial p}{\partial t} = -\frac{1}{q}(\nabla \cdot \boldsymbol{J_p}) - U_p \tag{7}$$

Solar spectra are included in the generation rate G through the Lambert-Beer's law, i.e. $\phi(\lambda) = \phi_0 e^{-\alpha(\lambda) z}$. Though this

law, the number of photons ($\phi(\lambda)$) of wavelength λ, per unit area and time, at a given point in the cell, can be computed. The term ϕ_0 is the incident photon flux, α is the absorption coefficient and z the spatial coordinate. Assuming that each photon leads to an electron-hole pair, dismissing reflection, it can be used to compute the generation rate G_0 in the following way. Taking the derivative with respect to z and integrating over λ, G_0 (in $cm^{-3}s^{-1}$) is obtained (Eq. 8) as a function of the absorption coefficient α (in cm^{-1}) and the position in the semiconductor. A similar process was used in [31].

$$G_0(z) = \int_0^{\infty} \alpha(\lambda)\phi(\lambda)e^{-\alpha(\lambda)\,z}d\lambda \tag{8}$$

To use the solar spectral irradiance, the absorption coefficient can be related to the extinction coefficient κ, by using $\alpha(\lambda) = 4\pi\kappa/\lambda$. The photon flux is linked to the solar spectral irradiance (F) via $\phi(\lambda) = \lambda F(\lambda)/(hc)$, where h is Planck's constant and c the speed of light in vacuum. The next step is to consider the metallized fraction (f_{met}) of the solar cells, which is the ratio of the covered area due to metallization, and the spectral reflection of the non-metallized region of the solar cell (R). When considering a bifacial cell with a front side metal fraction $f_{met,f}$ and a rear side metal fraction $f_{met,r}$, with the respective front and rear side spectral reflections, $R_f(\lambda)$ and $R_r(\lambda)$ and solar spectral irradiances $F_f(\lambda)$ and $F_r(\lambda)$, the generation rate G becomes (Eq. 9). To include illumination from the front and rear side, one needs to replace f_{met}, F and R accordingly (for the front or rear side).

$$G(z) = \frac{4\pi}{hc}(1 - f_{met})\int_{\lambda_1}^{\lambda_2} \kappa(\lambda)\, F(\lambda)\, e^{-\frac{4\pi\,\kappa\,z}{\lambda}}[1 - R(\lambda)]d\lambda \tag{9}$$

Losses due to Auger (R_{Auger}), trap-assisted (Schockley-Read-Hall, SRH) and band-to-band (R_D) recombination are included through Eq. 10, Eq. 11 and Eq. 12. In these equations, C_n,C_p and C are material constants, γ_n and γ_p are degeneracy factors obtained in terms of Fermi integrals, $n_{i,eff}$ is the intrinsic carrier concentration, τ_p and τ_n are hole and electron lifetimes respectively, and p_1 and n_1 are hole and electron expressions, depending on the trap energy level E_t. The intrinsic carrier concentration is obtained via ${n_{i,eff}}^2 = N_C N_V\, e^{-E_g/(k_B T)}$, where E_g is the semiconductor's bandgap.

$$R_{Auger} = (C_n + C_p)(np - \gamma_n\gamma_p n_{i,eff}^2) \tag{10}$$

$$R_{SRH} = \frac{np - \gamma_n\gamma_p n_{i,eff}^2}{\tau_p(n + n_1) + \tau_n(p + p_1)} \tag{11}$$

$$R_D = C(np - \gamma_n\gamma_p n_{i,eff}^2) \tag{12}$$

The n_1 and p_1 are defined as Eq. 13 and 14 shows, where ΔE_g the band gap narrowing energy, V_{th} is the thermal voltage and E_t is the trap energy level.

$$n_1 = \gamma_n\sqrt{N_C N_V}exp\left(-\frac{E_g - \Delta E_g}{2V_{th}}\right)\, exp\left(-\frac{\Delta E_t}{V_{th}}\right) \tag{13}$$

$$p_1 = \gamma_n\gamma_p\sqrt{N_C N_V}exp\left(-\frac{E_g - \Delta E_g}{2V_{th}}\right)\, exp\left(-\frac{\Delta E_t}{V_{th}}\right) \tag{14}$$

All these equations are implemented in the Semiconductor Module.

VI. RESULTS AND DISCUSSION

A. Measurement and simulation at standard conditions

The validation is discussed by comparing he measured and computed JV curve. See Table 3. The measurements were performed for the front and rear side of 6 solar cells leading to the standard deviations indicated in the table. Using the value of the series resistance $R_{ser} = 0.45\ \Omega cm^2$ from the experimental measurements, following results are found.

Table 3: Measured and calculated JV parameters.

	JV measurement		JV simulation	
Parameter	Front	Rear	Front	Rear
J_{sc} (mA/cm^2)	39.2 ± 0.03	34.6 ± 0.03	39.2	34.2
V_{oc} (mV)	653.1 ± 2	649.7 ± 2	646.4	654.6
P_{mpp} (W)	4.9 ± 0.02	4.3 ± 0.09	5.3	4.6
FF (%)	78.3 ± 0.2	78.2 ± 0.16	78.7	78.7
η (%)	20 ± 0.08	17.6 ± 0.1	20.0	18.0

According to the values in the table, relative differences ΔX for the parameter X were calculated as $\Delta X = (X_{calc} - X_{meas})/X_{meas}$, where "calc" and "meas" stand for calculated and measured, respectively. The J_{sc} and V_{oc} show relative differences between calculated and measured values, which are below 1% for the front side and below 2% for the rear side. The FF and efficiency exhibit relative differences below 1% for the front and rear side. The power P_{mpp} is the parameter experimenting the largest discrepance between measured and calculated values, being 8% for the front and 7% rear side. In summary, the error of the simulated JV parameters kept below 2%, except for power which reached values up to 8%, when illuminated with the reference solar spectrum AM1.5G.

B. Optimal parameters under illumination

As stated in the methodology, the optimization aimed to obtain maximum output power P_{mpp} for front side illumination at the AM1.5G standard and the AM1.08 spectrum, though the selected control parameters. The values for these parameters are summarized in Table 4. The genetic algorithm had the following inputs:

- Minimum and maximum values were defined to be
  - [0.2, 150, 0.2, 1e19, 1e14, 1e19] and
  - [1, 200, 1, 1e20, 1e15, 5e20].
  - The vectors refer to [d_E, d_{cell}, d_{BSF}, N_E, N_B, N_{BSF}].
- Population size (Npop): 70.
- Generation N° (Ngen): 110.
- Stop criterium (Nsic): 10.
- Mutation probability: 0.1.

In the following lines, an interpretation of the results is provided, based on solar cell physics.

Table 4: Optimal solar cell parameters under the standard AM1.5g and Atacama AM1.08 spectrum.

	Solar spectrum	
Parameter	AM1.5g	AM1.08
$d_E\ (\mu m)$	0.2002	0.2010
$d_{cell}\ (\mu m)$	150.5782	150.8933
$d_{BSF}\ (\mu m)$	0.7274	0.2539
$N_E\ (cm^{-3})$	9.8918×10^{19}	9.3597×10^{19}
$N_B\ (cm^{-3})$	9.8347×10^{14}	9.8475×10^{14}
$N_{BSF}\ (cm^{-3})$	3.8738×10^{20}	4.1179×10^{20}

Table 4 indicates that the emitter doping concentration is lower at AM1.08 compared to that at the standard spectrum. This result can be interpreted as a requirement due to enhanced recombination caused by the spectrum showing a high-power density (Atacama). A higher intensity means a larger number of photons impinging the solar cell, significantly increasing the excess minority carrier density and thus the Auger recombination [32] at the front side. Therefore, reducing the doping concentration is needed to keep recombination low enough.

Table 4 also shows that the thickness of the BSF is thinner and heavier doped at AM1.08 compared to the value at STC. The BSF has been documented to be linked to reducing the recombination at the rear side, by implementing a junction of same polarity (n-n^+) in this case [33], where the "+" denotes higher doping concentration. This behavior appears to be inverse to that at the emitter. However, for front side illumination, photons have been mostly absorbed in the emitter and base. Thus, there is no such requirement of limiting doping concentration at the rear side due to a lower excess minority carrier density compared to the levels at the front side. In such situation, the BSF needs to be thinner and heavier doped. From a broader perspective, studies regarding the optimum thickness for a phosphorus doped layer such as the BSF of the n-PERT solar cell indicate that for low doping concentration, the thickness is higher compared to that at higher doping concentration. In the latter, the thickness needs to be limited to avoid recombination [34]. These authors found that the optimal thickness for the P-doped layer is below 1 µm for doping concentrations from 5×10^{19} cm^{-3} to 1×10^{20} cm^{-3}, reaching highest efficiency in the range of 0.2 to 0.4 µm.

The thickness of the solar cell and doping of the substrate (base) appears to be not dependent on the solar spectrum used, resulting in the lower value of the interval, i.e. 150 µm and 9.83×10^{14} cm^{-3} at the standard and Atacama spectrum. From a theoretical point of view, current density can be enhanced by increasing the wafer thickness since it depends on the generation rate of electron-holes pairs, which in turn is defined as the z-dependent integral of Eq. 9. Nevertheless, the voltage decreases with the thickness as expressed by Eq. 15 [35], where W is the wafer thickness. The result obtained in this master work means that the voltage improves the efficiency more than what the current density could reduce it due to the thinner cell thickness.

$$\frac{dV_{oc}}{dW} = -\frac{kT}{q}\frac{1}{W} \tag{15}$$

Figure 7 shows the simulation of the optimized (full line) and non-optimized (dotted curve) n-PERT solar cell at AM1.5g (blue) and AM1.08 (red) solar spectrum. The calculation shows that for both spectra, the short circuit current density of the optimized solar cell is increased with respect to that value of the non-optimized cell, while keeping the open circuit voltage nearly at the same value. Thus, the power output is also increased. The implications of this result may reside that the global optimization performed through a genetic algorithm was successful in finding correct solar cell parameters in such a way of increasing the power though the current density and reducing recombination, when illuminated to two different solar spectra.

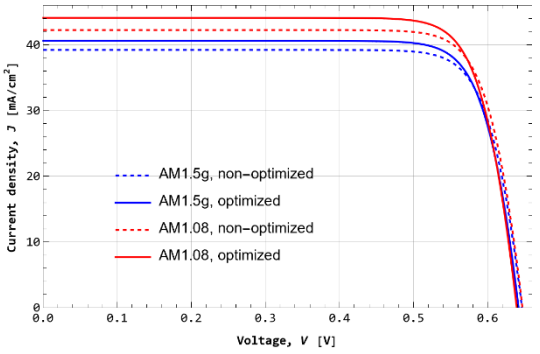

FIG. 7. Current-voltage characteristics of the optimized and non-optimized n-PERT solar cell at the AM1.5g and AM1.08 spectrum.

Based on the JV curves, Table 5 and Table 6 were created, showing the JV parameters of the optimized case and the non-optimized case. These information supports statement that all output electrical parameters improved, except the open circuit voltage, when considering the optimized solar cell compared to the non-optimized device.

Table 5: Output electrical parameters extracted from the optimized solar cell.

	J_{sc} (mA/cm^2)	V_{oc} (mV)	P_{mpp} (W)	η (%)
AM1.5g	40.6	641.7	5.5	21.5
AM1.08	44.1	639.2	5.9	23.4

Table 6: Output electrical parameters extracted from the non-optimized solar cell.

	J_{sc} (mA/cm^2)	V_{oc} (mV)	P_{mpp} (W)	η (%)
AM1.5g	39.2	646.4	5.3	20.0
AM1.08	42.2	647.0	5.7	21.6

To compare the results shown in Table 5 and Table 6, the relative difference was defined as 100 $(X_{opt} - X_{non\text{-}opt})/ X_{non\text{-}opt}$, where X is any of the electrical outputs. The term "opt" refers to optimal and "non-opt" to non-optimal value. The improvement of the optimized cell at AM1.5g with respect to the non-optimized case was +3.6% for J_{sc}, +4.3% for P_{mpp} and +7.6% for η; while a reduction of -0.7% for V_{oc} was observed. In the case of AM1.08 spectrum, the improvement of the optimized with respect to the non-optimized cell was +4.3% for J_{sc}, +4.7% for P_{mpp} and +8.5% for η; with a loss in V_{oc} of -1.2%. In turns out that the improvement is larger when illuminated under AM1.08 than at AM1.5g.

C. Performance for a whole day in Atacama Desert

Using the optimized values of the n-PERT solar cell at the AM1.08 solar spectrum, the Java code was implemented to calculate the performance of the cell during a whole day. FIG. 8, FIG. 9 and FIG. 10 depict J_{sc}, V_{oc} and P_{mpp} as a function of time, respectively. The characteristic shape of the curves is a consequence of the solar spectrum received at the front and rear side when the tilt angle is 20° with a north-south orientation and when the tilt angle is 90° with an east-west orientation. Therefore, the 20° angle exhibits the maximum irradiance at noon, whereas the maximum irradiance values for the 90° tilt angle case occur during the morning and afternoon.

It is seen that the curves for J_{sc} and P_{mpp} of the optimized case at 20° and 90° tilt angles are above those of the non-optimized cell. In the case of V_{oc} of the optimized cell, values lie slightly below those of the non-optimized cell.

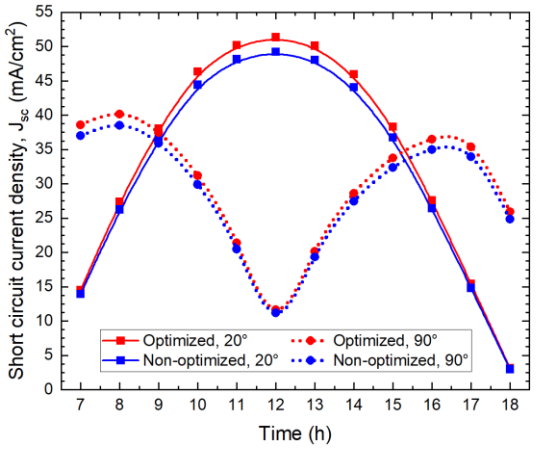

FIG. 8. Short circuit current density as function of time for the optimized and non-optimized solar cell at 20° and 90° tilt angles.

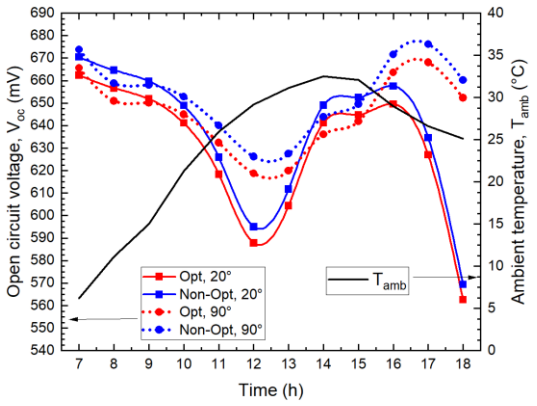

FIG. 9. Open circuit voltage as function of time for the optimized and non-optimized solar cell at 20° and 90° tilt angles.

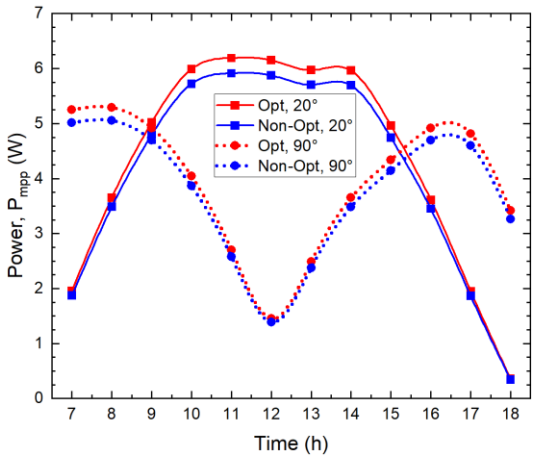

FIG. 10. Power as function of time for the optimized and non-optimized solar cell at 20° and 90° tilt angles.

V. CONCLUSIONS

In this work, a passivated emitter and rear totally diffused (n-PERT) crystalline silicon solar cell was modeled with the Semiconductor Module of COMSOL Multiphysics v6. The solar cell model is valid for a family of cases when the solar cell has the structure: p^+nn^+, where p^+ refers to the emitter, n stands for the base and n^+ corresponds to the back surface field (BSF). In addition, the model can be applied to monofacial and bifacial solar cells, for any illumination, i.e., only front, only rear, or simultaneous front and rear side illumination.

Using this model and a genetic algorithm (GA) implemented in MATLAB, 6 cell parameters were optimized for obtaining maximum output power. For this purpose, the LiveLink for MATLAB was used. The control parameters were the thickness of the emitter (d_E), cell (d_{cell}), and back surface field BSF (d_{BSF}) of the solar cell as well as the doping concentration of each layer, that is, N_E, N_{cell}, and N_{BSF}.

It turned out that the model combined with MATLAB allowed to optimize the device under a representative Atacama Spectrum having the air mass AM1.08. Optimization to the standard reference global solar spectrum AM1.5g was also carried out for comparison. Due to the differences between the Atacama and reference spectrum, the set of optimal parameters of the n-PERT solar cell resulted to be different. For instance, At AM1.08 the BSF needs to be thinner and lightly doped compared to values at AM1.5g. In addition, the doping of the emitter should be heavier compared to the doping at AM1.5g. Overall, the optimized cell led to a gain of +4.3% for the short circuit current density J_{sc}, +4.7% for the power P_{mpp} and +8.5% for the efficiency η; with a loss in the open circuit voltage V_{oc} of -1.2%.

The COMSOL model combined with Java allowed to calculate the performance for a whole day in Atacama Desert, during a summer solstice. This calculation was carried for the optimized n-PERT cell to AM1.08 at two configurations: (i) tilt angle of 20° with a north-south orientation and (ii) tilt angle of 90° with an east-west orientation. Curves of J_{sc}, P_{mpp} and η of the optimized cell lie above those of the non-optimized cell. The V_{oc} over time of the optimized cell did not change significantly with respect to that of the non-optimized case, showing that the GA led to minimizing recombination phenomena.

ACKNOWLEDGMENTS

The authors gratefully acknowledge the technical and academic support of the Master's Degree in Numerical Simulation in Science and Engineering with COMSOL Multiphysics (www.multifisica.uma.es).

REFERENCES

[1] Solar GIS: Global Horizontal Irradiation, (2022). https://solargis.com/es/maps-and-gis-data/download/world (accessed February 16, 2022).

[2] R.A. Escobar, C. Cortés, A. Pino, M. Salgado, E.B. Pereira, F.R. Martins, J. Boland, J.M. Cardemil, Estimating the potential for solar energy utilization in Chile by satellite-derived data and ground station measurements, Sol. Energy. 121 (2015) 139–151. doi:10.1016/j.solener.2015.08.034.

[3] R.A. Escobar, C. Cortés, A. Pino, E.B. Pereira, F.R. Martins, J.M. Cardemil, Solar energy resource assessment in Chile: Satellite estimation and ground station measurements, Renew. Energy. 71 (2014) 324–332. doi:10.1016/J.RENENE.2014.05.013.

[4] R. Rondanelli, A. Molina, M. Falvey, R. Rondanelli, A. Molina, M. Falvey, The Atacama Surface Solar Maximum, Bull. Am. Meteorol. Soc. 96 (2015) 405–418. doi:10.1175/BAMS-D-13-00175.1.

[5] ASTM, ASTM International - Standards Worldwide, (2017). https://www.astm.org/ (accessed February 15, 2022).

[6] D.R. Myers, K. Emery, C. Gueymard, Revising and Validating Spectral Irradiance Reference Standards for Photovoltaic Performance, in: ASES/ASME Sol. 2002 Conf., 2002: pp. 567–574. doi:https://doi.org/10.1115/1.1638784.

[7] C.A. Gueymard, Parameterized transmittance model for direct beam and circumsolar spectral irradiance, Sol. Energy. 71 (2001) 325–346. doi:10.1016/S0038-092X(01)00054-8.

[8] C. Gueymard, SMARTS: Simple Model of the Atmospheric Radiative Transfer of Sunshine | Grid Modernization | NREL, 1995. https://www.nrel.gov/grid/solar-resource/smarts.html (accessed March 23, 2019).

[9] A. Marzo, P. Ferrada, F. Beiza, P. Besson, J. Alonso-Montesinos, J. Ballestrín, R. Román, C. Portillo, R. Escobar, E. Fuentealba, Standard or local solar spectrum? Implications for solar technologies studies in the Atacama desert, Renew. Energy. (2018). doi:10.1016/j.renene.2018.05.039.

[10] J.F. Lelièvre, R. Couderc, N. Pinochet, L. Sicot, D. Munoz, R. Kopecek, P. Ferrada, A. Marzo, D. Olivares, F. Valencia, E. Urrejola, Desert label development for improved reliability and durability of photovoltaic modules in harsh desert conditions, Sol. Energy Mater. Sol. Cells. 236 (2022). doi:10.1016/j.solmat.2021.111508.

[11] L.C.H. and N.J. Ekins-Daukes, Fundamental losses in solar cells, Prog. Photovolt Res. Appl. 19 (2010) 286–293. doi:10.1002/pip.

[12] O. Dupré, R. Vaillon, M.A. Green, Physics of the temperature coefficients of solar cells, Sol. Energy Mater. Sol. Cells. 140 (2015) 92–100. doi:10.1016/j.solmat.2015.03.025.

[13] ITRPV 2021, International Technology Roadmap of Photovoltaicos (ITRPV), 2021.

[14] R. Kopecek, J. Libal, Bifacial photovoltaics 2021: Status, opportunities and challenges, Energies. 14 (2021). doi:10.3390/en14082076.

[15] P. Ferrada, D. Rudolph, C. Portillo, A. Adrian, J. Correa-Puerta, R. Sierpe, V. del Campo, M. Flores, T.P. Corrales,

R. Henríquez, M.J. Kogan, J. Lossen, Interface analysis of Ag/n-type Si contacts in n-type PERT solar cells, Prog. Photovoltaics Res. Appl. (2020) pip.3242. doi:10.1002/pip.3242.

[16] A. Edler, Development of bifacial n-type solar cells for industrial application, Universität Konstanz, 2014. http://nbn-resolving.de/urn:nbn:de:bsz:352-275017.

[17] A. Fell, K.R. McIntosh, P.P. Altermatt, G.J.M. Janssen, R. Stangl, A. Ho-Baillie, H. Steinkemper, J. Greulich, M. Muller, B. Min, K.C. Fong, M. Hermle, I.G. Romijn, M.D. Abbott, Input Parameters for the Simulation of Silicon Solar Cells in 2014, IEEE J. Photovoltaics. 5 (2015) 1250–1263. doi:10.1109/JPHOTOV.2015.2430016.

[18] P. Ferrada, A. Marzo, E. Cabrera, H. Chu, J. Rabanal, D. Diaz-almeida, A. Schneider, R. Kopecek, Potential for photogenerated current for silicon based photovoltaic modules in the Atacama Desert, Sol. Energy. 144 (2017) 580–593. doi:10.1016/j.solener.2017.01.053.

[19] A. Edler, V.D. Mihailetchi, L.J. Koduvelikulathu, C. Comparotto, R. Kopecek, R. Harney, Metallization–induced recombination losses of bifacial silicon solar cells, Prog. Photovoltaics Res. Appl. 23 (2015) 620–627. doi:10.1002/PIP.2479.

[20] L.H. Slooff, B. Brockholz, W.J.H. Verhees, S.C. Veenstra, E.M. Cobussen-Pool, J.M. Kroon, E.E. Bende, Determination of the intrinsic diode parameters of polymer solar cells, Energy Procedia. 31 (2012) 11–20. doi:10.1016/j.egypro.2012.11.159.

[21] M.A. Green, Solar cell fill factors: General graph and empirical expressions, Solid State Electron. 24 (1981) 788–789. doi:10.1016/0038-1101(81)90062-9.

[22] S. Katoch, S.S. Chauhan, V. Kumar, A review on genetic algorithm: past, present, and future, Multimed. Tools Appl. 80 (2021) 8091–8126. doi:10.1007/s11042-020-10139-6.

[23] J.A. Vasconcelos, R.R. Saldanha, L. Krähenbühl, A. Nicolas, Genetic algorithm coupled with a deterministic method for optimization in electromagnetics, IEEE Trans. Magn. 33 (1997) 1860–1863. doi:10.1109/20.582645.

[24] T. Liu, L. Ye, H. Chen, J. Li, Z. Wu, R. Zhou, A combined steepest descent and genetic algorithm (SD/GA) approach for the optimization of solvation parameters, Mol. Simul. 32 (2006) 427–435. doi:10.1080/08927020600812672.

[25] C.A. Gueymard, The SMARTS spectral irradiance model after 25 years: New developments and validation of reference spectra, Sol. Energy. 187 (2019) 233–253. doi:10.1016/j.solener.2019.05.048.

[26] P. Ferrada, S. Rodríguez, A. Marzo, M. Ruiz Ferrández, B. Ivorra, E. Ruiz Reina, F. E, Performance Simulation of n-PERT Solar Cell and 1- Cell mini Module for Atacama Desert Conditions, in: 8th World Conf. Photovolt. Energy Convers., Milan, Italy, 2022.

[27] T. Katsaounis, K. Kotsovos, I. Gereige, A. Basaheeh, M. Abdullah, A. Khayat, Performance assessment of bifacial c-Si PV modules through device simulations and outdoor measurements, Renew. Energy. 143 (2019) 1285–1298. doi:10.1016/j.renene.2019.05.057.

[28] P.P. Altermatt, Models for numerical device simulations of crystalline silicon solar cells - A review, J. Comput. Electron. 10 (2011) 314–330. doi:10.1007/s10825-011-0367-6.

[29] N.D. Arora, J.R. Hauser, D.J. Roulston, Electron and Hole Mobilities in Silicon as a Function of Concentration and Temperature, IEEE Trans. Electron Devices. 29 (1982) 292–295. doi:10.1109/T-ED.1982.20698.

[30] C. Multiphysics, Semiconductor Module: User's Guide, 2018.

[31] M.M. Chowdhury, B. Debnath, Approximation of carrier generation rate in common solar cells and studies for optimization of n+p silicon solar cell for AM1.5G and AM1.5D, in: 2012 7th Int. Conf. Electr. Comput. Eng. ICECE 2012, 2012: pp. 327–330. doi:10.1109/ICECE.2012.6471553.

[32] R.A. Sinton, R.M. Swanson, Recombination in Highly Injected Silicon, IEEE Trans. Electron Devices. 34 (1987) 1380–1389. doi:10.1109/T-ED.1987.23095.

[33] S.R. Dhariwal, A.P. Kulshreshtha, Theory of back surface field silicon solar cells, Solid State Electron. 24 (1981) 1161–1165. doi:10.1016/0038-1101(81)90185-4.

[34] N. Stem, M. Cid, Studies of phosphorus Gaussian profile emitter silicon solar cells, Mater. Res. 4 (2001) 143–148. doi:10.1590/s1516-14392001000200018.

[35] R. Brendel, H.J. Queisser, On the thickness dependence of open circuit voltages of p-n junction solar cells, Sol. Energy Mater. Sol. Cells. 29 (1993) 397–401. doi:10.1016/0927-0248(93)90098-N.